The Astrophysical Journal, 601:905–920, 2004 February 1

THERMAL AND MAGNETOROTATIONAL INSTABILITY IN THE INTERSTELLAR MEDIUM: TWO-DIMENSIONAL NUMERICAL SIMULATIONS

Robert A. Piontek and Eve C. Ostriker
Department of Astronomy, University of Maryland, College Park, MD 20742-2421; rpiontek@astro.umd.edu, ostriker@astro.umd.edu
Received 2003 August 25; accepted 2003 October 6

ABSTRACT

The structure and dynamics of diffuse gas in the Milky Way and other disk galaxies may be strongly influenced by thermal and magnetorotational instabilities (TI and MRI, respectively) on scales $\sim$1–100 pc. We initiate a study of these processes, using two-dimensional numerical hydrodynamic and magnetohydrodynamic simulations with conditions appropriate for the atomic interstellar medium (ISM). Our simulations incorporate thermal conduction and adopt local "shearing-periodic" equations of motion and boundary conditions to study dynamics of a $(100\ \mathrm{pc})^2$ radial-vertical section of the disk. We demonstrate, consistent with previous work, that nonlinear development of "pure TI" produces a network of filaments that condense into cold clouds at their intersections, yielding a distinct two-phase warm/cold medium within $\sim$20 Myr. TI-driven turbulent motions of the clouds and warm intercloud medium are present but saturate at quite subsonic amplitudes for uniform initial $P/k = 2000\ \mathrm{K\ cm^{-3}}$. MRI has previously been studied in near-uniform media; our simulations include both TI+MRI models, which begin from uniform-density conditions, and cloud+MRI models, which begin with a two-phase cloudy medium. Both the TI+MRI and cloud+MRI models show that MRI develops within a few galactic orbital times, just as for a uniform medium. The mean separation between clouds can affect which MRI mode dominates the evolution. Provided intercloud separations do not exceed half the MRI wavelength, we find the MRI growth rates are similar to those for the corresponding uniform medium. This opens the possibility that if low cloud volume filling factors increase MRI dissipation times compared to those in a uniform medium, then MRI-driven motions in the ISM could reach amplitudes comparable to observed H I turbulent line widths.

Subject headings: galaxies: ISM — instabilities — ISM: kinematics and dynamics — ISM: magnetic fields — MHD

On-line material: color figures, mpeg animation

1. INTRODUCTION

The Galactic interstellar medium (ISM) is characterized by complex spatial distributions of density, temperature, and magnetic fields, as well as a turbulent velocity field that animates the whole system. The relative proportions of ISM gas in different thermal/ionization phases, and their respective dynamical states, may reflect many contributing physical processes of varying importance throughout the Milky Way (or external galaxies). Even considering just the Galaxy's atomic gas component, observable in H I emission and absorption, a wide variety of temperatures and pervasive high-amplitude turbulence is inferred (Heiles & Troland 2003), and a number of different physical processes may collude or compete in establishing these conditions.

In the traditional picture of the ISM, turbulence in atomic gas is primarily attributed to the lingering effects of supernova blast waves that sweep through the ISM (Cox & Smith 1974; McKee & Ostriker 1977; Spitzer 1978). Densities and temperatures of atomic gas are expected to lie preferentially near either the warm or cold stable thermal equilibria available given heating primarily by the photoelectric effect on small grains (Wolfire et al. 1995, 2003). Thermal instability (TI) is believed to play an important role in maintaining gas near the stable equilibria (Field 1965).

Certain potential difficulties with this picture motivate an effort to explore effects not emphasized in the traditional model. In particular, because energetic stellar inputs are intermittent in space and time, while turbulence is directly or indirectly inferred to pervade the whole atomic ISM, it is valuable to assess alternative spatially/temporally *distributed* turbulent driving mechanisms. Candidate mechanisms recently proposed for driving turbulence include both TI (Koyama & Inutsuka 2002; Kritsuk & Norman 2002a, 2002b) and the magnetorotational instability (MRI; Sellwood & Balbus 1999; Kim, Ostriker, & Stone 2003). In addition to uncertainties about the source of turbulence in H I gas, other puzzles surrounding H I temperatures (e.g., Kalbera, Schwarz, & Goss 1985; Verschuur & Magnani 1994; Spitzer & Fitzpatrick 1995; Fitzpatrick & Spitzer 1997) have grown more pressing with recent observations (Heiles 2001; Heiles & Troland 2003). Namely, the Heiles & Troland observations suggest that significant H I gas ($\gtrsim$48%) could be in the thermally unstable temperature regime between 500 and 5000 K. Using observational evidence from various tracers, Jenkins (2003) has also recently argued that very large pressures and other large departures from dynamical and thermal equilibrium are common in the ISM and indicate rapid changes likely driven by turbulence. To assess and interpret this evidence theoretically, it is necessary to understand the nonlinear development of TI, the effects of independent dynamical ISM processes on TI, and the ability in general of magnetohydrodynamic (MHD) turbulence to heat and cool ISM gas via shocks, compressions, and rarefactions.

In recent years, direct numerical simulation has become an increasingly important tool in theoretical investigation of the ISM's structure and dynamics and has played a key role in promoting the increasingly popular notion of the ISM as a

"phase continuum." In MHD (or hydrodynamic) simulations, the evolution of gas in the computational domain is formalized in terms of time-dependent flow equations with appropriate source terms to describe externally imposed effects. Fully realistic computational ISM models will ultimately require numerical simulations with a comprehensive array of physics inputs. Recent works toward this goal that address turbulent driving and temperature/density probability distribution functions (PDFs) include the three-dimensional simulations of Korpi et al. (1999), de Avillez (2000), Wada (2001), and Mac Low et al. (2001) and the two-dimensional simulations of Rosen & Bregman (1995), Wada, Spaans, & Kim (2000), Wada & Norman (2001), and Gazol et al. (2001). Among other physics inputs, all of these simulations include modeled effects of star formation, with either supernova-like or stellar-like localized heating events that lead to expanding flows. For some of these models, the cooling functions also permit TI in certain density regimes.

Since many of the individual processes affecting the ISM's structure and dynamics are not well understood, in addition to comprehensive physical modeling, it is also valuable to perform numerical simulations that focus more narrowly on a single process or on a few processes that may potentially interact strongly. This controlled approach can yield significant insight into the relative importance of multiple effects in complex systems, such as the ISM. Using models that omit supernova and stellar energy inputs, it is possible to sort out, for example, whether the appearance of phase continua in density/temperature PDFs requires localized thermal energy inputs or can develop simply from the disruption of TI by moderate-amplitude turbulence, such as that driven by MRI.

Recent simulations that have focused on the nonlinear development of TI under ISM conditions include Hennebelle & Pérault (1999), Burkert & Lin (2000), Vázquez-Semadeni, Gazol, & Scalo (2000), Sánchez-Salcedo, Vázquez-Semadeni, & Gazol (2002), Kritsuk & Norman (2002a, 2002b), and Vázquez-Semadeni et al. (2003). Previous simulations of MRI in two and three dimensions have focused primarily on the situation in which the density is relatively uniform, for application to accretion disks (e.g., Hawley & Balbus 1992; Hawley, Gammie, & Balbus 1995; Stone et al. 1996). In recent work, Kim et al. (2003) began study of MRI in the galactic context using isothermal simulations, focusing on dense cloud formation due to the action of self-gravity on turbulently compressed regions.

In this work, we initiate a computational study aimed at understanding how density, temperature, velocity, and magnetic field distributions would develop in the diffuse ISM in the absence of localized stellar energy input. Of particular interest is the interaction between TI and MRI. TI tends to produce a cloudy medium, and this cloudy medium may affect both the growth rate of MRI and its dissipation rate, and hence the saturated-state turbulent amplitude that is determined by balancing these rates. On the other hand, the turbulence produced by MRI may suppress and/or enhance TI by disrupting and/or initiating the growth of dense condensations. Evaluation of quasi–steady-state properties such as the mean turbulent velocity amplitude and the distribution of temperatures will await three-dimensional simulations. In the present work, which employs two-dimensional simulations, we focus on evaluation of our code's performance for studies of thermally bistable media and analysis of nonlinear development in models of pure TI, TI together with MRI, and MRI in a medium of preexisting clouds.

In § 2, we describe our numerical methods and code tests. In § 3, we present results from simulations of thermally unstable gas without magnetic fields, and in § 4 we present results of models in which magnetic fields and sheared rotation have been added so that MRI occurs. Finally, in § 5, we summarize our results, discuss their implications, and make comparisons to previous work.

2. NUMERICAL METHODS

2.1. *Model Equations and Computational Algorithms*

We integrate the time-dependent equations of MHD using a version of the ZEUS-2D code (Stone & Norman 1992a, 1992b). ZEUS uses a time-explicit, operator-split, finite difference method for solving the MHD equations on a staggered mesh, capturing shocks via an artificial viscosity. Velocities and magnetic field vectors are face-centered, while energy and mass density are volume-centered. ZEUS employs the CT and MOC algorithms (Evans & Hawley 1988; Hawley & Stone 1995) to maintain $\nabla \cdot \boldsymbol{B} = 0$ and ensure accurate propagation of Alfvén waves.

For the present study, we have implemented volumetric heating and cooling terms, and a thermal conduction term. We also model the differential rotation of the background flow and the variation of the stellar/dark matter gravitational potential in the local limit with $x \equiv R - R_0 \ll R_0$, where R_0 is the Galactocentric radius of the center of our computational domain. The equations we solve are therefore

$$\frac{\partial \rho}{\partial t} + \nabla \cdot (\rho \boldsymbol{v}) = 0, \tag{1}$$

$$\frac{\partial \boldsymbol{v}}{\partial t} + \boldsymbol{v} \cdot \nabla \boldsymbol{v} = -\frac{\nabla \boldsymbol{P}}{\rho} + \frac{1}{4\pi\rho} (\nabla \times \boldsymbol{B}) \times \boldsymbol{B} + 2q\Omega^2 x \hat{\boldsymbol{x}} - 2\Omega \times \boldsymbol{v}, \tag{2}$$

$$\frac{\partial \mathcal{E}}{\partial t} + \boldsymbol{v} \cdot \nabla \mathcal{E} = -(\mathcal{E} + P) \nabla \cdot \boldsymbol{v} - \rho \mathcal{L} + \nabla \cdot (\mathcal{K} \nabla T), \tag{3}$$

$$\frac{\partial \boldsymbol{B}}{\partial t} = \nabla \times (\boldsymbol{v} \times \boldsymbol{B}). \tag{4}$$

All symbols have their usual meanings. We use an ideal gas law $\mathcal{E} = P\gamma^{-1}$ with $\gamma = 5/3$. The net cooling per unit mass is given by $\mathcal{L} = \rho\Lambda(\rho,\ T) - \Gamma$. We adopt the simple atomic ISM heating and cooling prescriptions of Sánchez-Salcedo et al. (2002), in which the cooling function, $\Lambda(\rho,\ T)$, is a piecewise power-law fit to the detailed models of Wolfire et al. (1995). The heating rate, Γ, is taken to be constant at 0.015 ergs s^{-1} g^{-1}. In the tidal potential term of equation (2), $q \equiv -d \ln \Omega / d \ln R$ is the local dimensionless shear parameter, equal to unity for a flat rotation curve in which the angular velocity $\Omega \propto R^{-1}$.

The present set of simulations is two-dimensional, with the computational domain representing a square sector in the radial-vertical (x-z) plane. In the local frame, the azimuthal direction $\hat{\boldsymbol{\phi}}$ becomes the $\hat{\boldsymbol{y}}$ coordinate axis; y-velocities and magnetic field components are present in our models, but $(\partial/\partial y) = 0$ for all variables. To reduce diffusion from advection in the presence of background shear, we apply the velocity decomposition method of Kim & Ostriker (2001). We employ periodic boundary conditions in the $\hat{\boldsymbol{z}}$-direction and shearing-periodic boundary conditions in the $\hat{\boldsymbol{x}}$-direction (Hawley &

Balbus 1992; Hawley et al. 1995). This framework allows us to incorporate realistic galactic shear, while avoiding numerical artifacts associated with simpler boundary conditions.

Because cooling times can be very short, the energy equation update from the net cooling terms is solved implicitly using Newton-Raphson iteration. At the start of each iteration the time step is initially computed from the CFL condition using the sound speed, Alfvén speed, and conduction parameter. This is followed by a call to the cooling subroutine. The change in temperature within each zone is limited to 10% of its initial value. If this requirement is not met for all cells in the grid, the time step is reduced by a factor of 2, and the implicit energy update is recalculated. Tests with our cooling function show that this time step restriction could in principle become quite prohibitive if zones were far from thermal equilibrium. In practice, however, for our model simulations this is typically not the case, and the time step is reduced once or twice at most.

The update from the conduction operator is solved explicitly, using a simple five-point stencil for the spatial second derivative of temperature (cf. Press et al. 1992, eq. [19.2.4]). In two dimensions, the CFL condition is $\Delta t < (\Delta x)^2[nk/(\gamma - 1)]/(4\mathcal{K})$. As Koyama & Inutsuka (2003) have recently pointed out, the importance of incorporating conduction in simulations that contain thermally unstable gas has been occasionally overlooked in past work. Without conduction, the growth rates for TI are largest at the smallest scales, and unresolved growth at the grid scale may occur.[1] The inclusion of conduction, however, has a stabilizing effect on TI at small scales, and the conduction parameter can be adjusted to allow spatial resolution of TI on the computational grid. Here we treat $\mathcal{K}$ as a parameter that may be freely specified for numerical efficacy; we discuss the physical level of conduction in the ISM below.

2.2. *Code Tests*

The ZEUS MHD code has undergone extensive numerical testing and has been used in a wide variety of astrophysical investigations. In addition, we have tested the code without cooling and conduction and have found it can accurately reproduce the linear growth rates of the MRI for an adiabatic medium (see also Hawley & Balbus 1992). To test our implementation of the heating, cooling, and conduction terms, we performed one-dimensional simulations to compare with the linear growth rates of the TI (Field 1965). The models were initialized with eigenmodes of the instability, and three levels of conduction were chosen: $\mathcal{K} \in (7.48 \times 10^6,\ 7.48 \times 10^7,\ 7.48 \times 10^8)$ ergs cm^{-1} K^{-1} s^{-1}. For these tests, the grid was 128 zones, and the box size was $L = 100$ pc. The initial density and pressure were set to $n = 0.79$ cm^{-3} and $P/k = 2000$ cm^{-3} K, implying corresponding cutoffs for TI ("Field length"), $\lambda_F \in \{2.7,\ 8.4,\ 27\}$ pc for our adopted cooling function (see § 3.1).[2] In Figure 1 we plot the growth rates from the simulations on top of the analytic curves. The numerical growth rates are obtained by measuring the logarithmic rate of change of the maximum density. The agreement between the analytic and numerical growth rates is quite good. This test confirms that the newly added cooling and conduction subroutines are working correctly and is critical in assessing the performance of the code as applied to multiphase ISM simulations. Note that at small scales TI is essentially isobaric, so that this test demonstrates the ability of the code to maintain near-uniform pressure via hydrodynamic flow to compensate for changes in temperature driven by the cooling term (see eq. [3]).

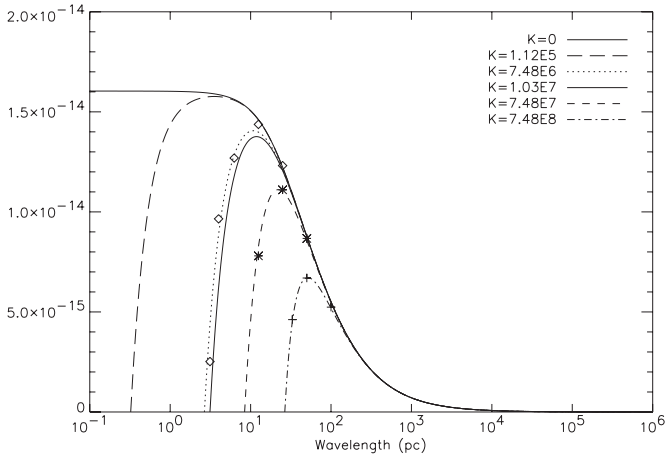

FIG. 1.—Theoretical TI growth rates (Field 1965) for varying levels of conduction $\mathcal{K} = 7.48 \times 10^6,\ 10^7,$ and 10^8 ergs cm^{-1} K^{-1} s^{-1} (*dotted, dashed, and dash-dotted curves, respectively*), overlaid with measured growth rates (*points*) from test simulations. For reference we include the theoretical curves for $\mathcal{K} = 0$ (*solid curve*) and for our chosen value of $\mathcal{K} = 1.03 \times 10^7$ ergs cm^{-1} K^{-1} s^{-1} (*triple-dot–dashed curve*), as well as using an estimate of the physical conduction in the ISM at 2000K, $\mathcal{K} = 1.12 \times 10^5$ ergs cm^{-1} K^{-1} s^{-1} (*long-dashed curve*). The asymptotic growth rate at small scales is (2 Myr)$^{-1}$ for the adopted parameters.

By comparison with simulations in which we set $\mathcal{K} = 0$, tests with nonzero $\mathcal{K}$ also confirm that conduction provides a needed numerical stabilization. When conduction is omitted, growth rates for TI will always be greatest at the largest available wavenumbers. Our two-dimensional tests with $\mathcal{K} = 0$ have confirmed this is indeed the case: simulations in which TI is seeded from random perturbations form high-density clouds that are the size of a single grid zone. Further two-dimensional tests show that provided λ_F is resolved by at least eight zones, this grid-scale growth is suppressed. For the models we present, the conduction parameter and grid resolution were chosen such that we can adequately resolve all modes for which TI is unstable.

Because we are modeling a medium containing very large density contrasts, it is desirable to assess the evolution of contact discontinuities between the high- and low-density regions, representing cold and warm phases in pressure equilibrium. The diffusive smearing of contact discontinuities is an inherent limitation of all finite difference codes, but the numerical problem can be magnified with the inclusion of a thermally bistable net cooling function. As these contact discontinuities are advected through the grid, upstream and downstream zones adjacent to the discontinuity are set to intermediate densities that may be thermally unstable. Thermally unstable gas adjoining the initial contact rapidly heats or cools to reach a pressure different from the initial equilibrium, and this can potentially introduce additional dynamics to the problem.

To explore this numerical issue for the problem at hand, we have performed one-dimensional advection tests of relaxed profiles of high-density clouds in a low-density ambient

[1] Similar numerical difficulties arise if the Jeans scale is not resolved in simulations of self-gravitating clouds (Truelove et al. 1997).

[2] The Field length is $\lambda_F = 2\pi\{(\rho^2\Lambda/\mathcal{K}T)[1 - (\partial \ln \Lambda/\partial \ln T)]\}^{-1/2}$ when $\Lambda =$ function of T.

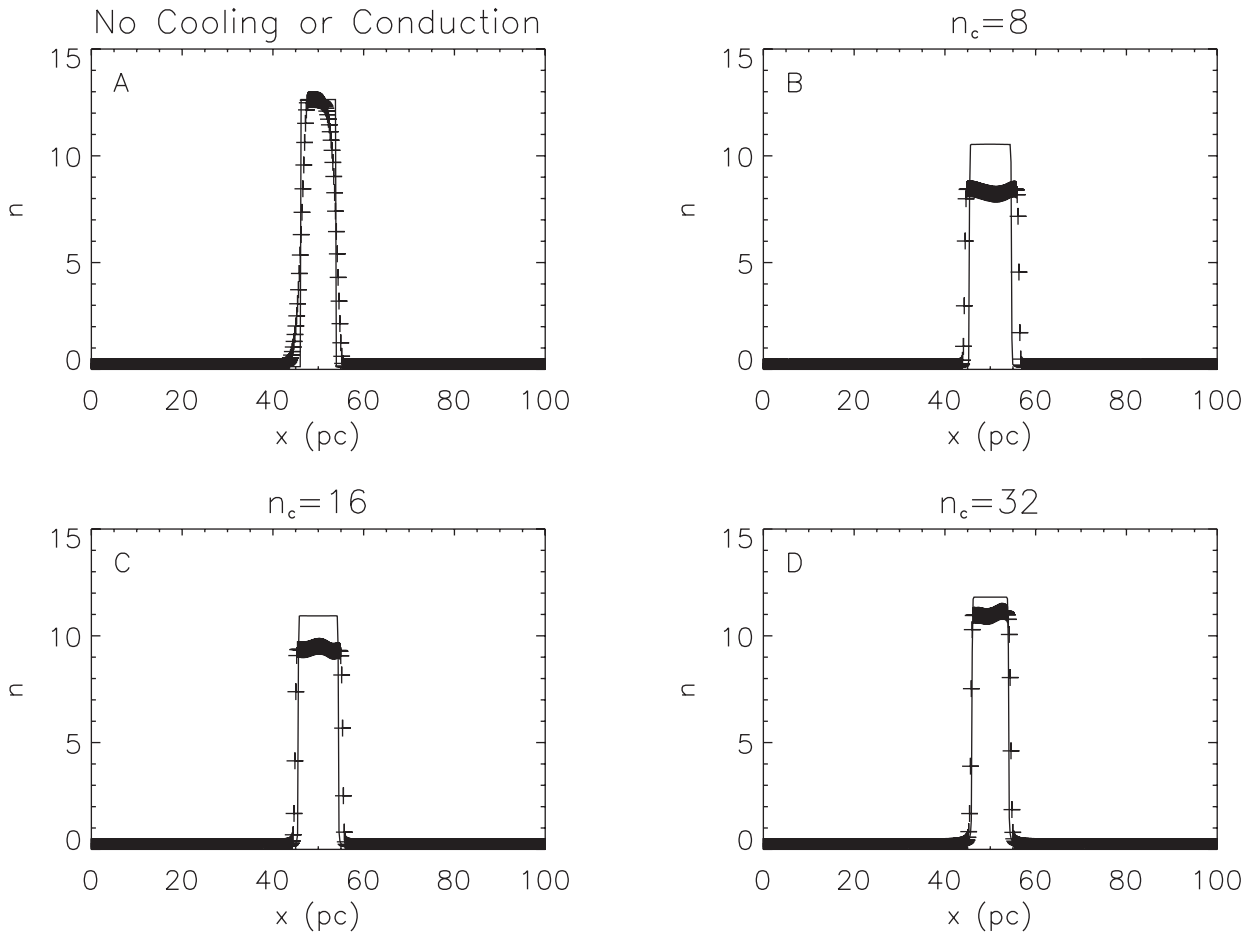

FIG. 2.—Advection test results (*plus signs*) compared with the initial profile (*solid line*) of a one-dimensional cloud. (*a*) We show results from the original ZEUS-2D code, without cooling and conduction. (*b–d*) We set the conduction parameter so that $n_c = 8$, 16, and 32, respectively. Advection test results improve as n_c increases.

medium. The resolution is 512 zones for all runs. We define $n_c \equiv \lambda_F/\delta x$, i.e., the number of zones in a Field length at the mean density, giving a measure of the resolution at scales for which conduction is important. We vary $\mathcal{K}$ so that n_c varies from 8 to 32 in powers of 2. The initial conditions consist of a top-hat function of high and low density set to be in approximate pressure equilibrium. The exact equilibrium state is the solution of $\rho\mathcal{L} = \nabla\cdot(\mathcal{K}\nabla T)$ from equation (3) and is different for each value of $\mathcal{K}$. Initial oscillations in pressure, velocity, and density gradually decay, and we consider the profile to be relaxed when these oscillations reach approximately 1% of their value early in the simulation. After a relaxed "cloud" profile is achieved, the velocity of all cells is set to a constant value comparable to the sound speed, and the "cloud" is advected through the grid twice. Profiles at the end of these runs are compared to the initial relaxed equilibrium profile in Figure 2. Note that as n_c increases, so does the number of zones over which the contact discontinuity is spread; the results clearly show that the profile is preserved more faithfully as n_c increases from 8 to 32. For comparison we also show results from the original ZEUS-2D code, without conduction and cooling.

It is clear that running higher levels of conduction at a given resolution has the advantage of smearing contact discontinuities over an increasing number of zones, thus improving the performance of the code in the advection tests. However, increasing $\mathcal{K}$ has the disadvantage of inhibiting TI at larger and larger spatial scales, such that only very large scale structures can develop from TI. As we are interested in how wavelengths of growing MRI modes in a cloudy medium may be affected by the distances between condensations, it is undesirable to limit the available dynamic range for this exploration. For $n_c = 32$ at a resolution of 256 zones, λ_F is 12.5 pc, and the maximum TI growth rate occurs at 29 pc, about one-third of our box. A second disadvantage of increasing $\mathcal{K}$ is that conduction quickly begins to set the time step for the simulations. So we make the practical choice of setting $n_c = 8$. At resolution of 256^2, and a box size of 100 pc, we then set $\mathcal{K} = 1.03 \times 10^7$ ergs cm^{-1} K^{-1} s^{-1}, to yield $\lambda_F = 3.125$ pc. This compromise choice allows us to resolve TI developing from the initial conditions, to maintain advection profiles within $\sim$20%, and to have adequate numbers and resolution of the condensations that form to represent a cloudy medium in a meaningful way.

The true thermal conduction level in the ISM is not well known observationally and must be affected by the fractional ionization (since electrons are highly mobile when present) and magnetic field geometry. A minimum level of conduction for the atomic ISM is that of neutral hydrogen gas, $\mathcal{K} = 2.5\times 10^3\ T^{1/2}$ ergs cm^{-1} K^{-1} s^{-1} (Parker 1953). At 2000 K, $\mathcal{K} = 1.1 \times 10^5$ ergs cm^{-1} K^{-1} s^{-1}, about a factor of 100 smaller than our value, such that λ_F would be reduced by a factor of $\sim$10. The use of a smaller conduction parameter would not, however, significantly alter our main results. The most unstable

wavelength for TI (see Fig. 1) would be significantly smaller, 3 pc compared to 12 pc for our adopted $\mathcal{K}$, which would reduce the size scale of the clouds in the initial condensation phase. However, the growth rate of TI for the most unstable wavelength would increase by only 15% compared to our models. The evolution toward more massive clouds via agglomeration would proceed similarly to the results we have found. In addition, the overall tendency to maintain a two-phase medium after TI has developed, as well as the characteristics we identify for MRI growth in a cloudy medium, would not be affected by the initial sizes of clouds that form.

3. THERMAL INSTABILITY SIMULATIONS

3.1. *Physical Principles and Timescales*

Various heating and cooling processes in the ISM define a thermal equilibrium pressure-density curve on which energy is radiated at the same rate it is absorbed. Perturbations from the equilibrium curve will either be stable or unstable depending on its local shape (Field, Goldsmith, & Habing 1969). Our adopted equilibrium curve (Vázquez-Semadeni et al. 2000) is shown in Figure 4 (together with contours of temperature corresponding to transitions in the cooling function, and with scatter plots from our first simulation). Gas in the region above the curve has net cooling ($\mathcal{L} > 0$) and gas below the curve has net heating ($\mathcal{L} < 0$). When gas on the equilibrium curve in the warm phase (phase "F," at $T > 6102$ K) is perturbed to higher (lower) temperatures, there is net cooling (heating), and the gas returns to equilibrium. The same situation applies to gas in the cold phase (phase "H," at $T < 141$ K). At intermediate temperatures (phase "G," 313 K $< T <$ 6102 K), however, perturbations from equilibrium to higher (lower) temperatures results in net heating (cooling), and the gas continues heating (cooling) until it reaches equilibrium in phase F (H). This is the physical basis for TI, which was first analyzed comprehensively by Field (1965).

TI has long been believed to play an important role in structuring the ISM because at typical volume-averaged atomic densities estimated for the ISM (e.g., $n_{\rm H\,I} = 0.57$ from Dickey & Lockman 1990) gas in thermal equilibrium would lie on the unstable portion of the curve. Thus, much of the mass of the ISM in the Milky Way and similar galaxies is believed to be in cold clouds or a warm intercloud medium, the two stable neutral atomic phases (e.g., Wolfire et al. 2003). Recent theoretical work has emphasized that dynamical processes may drive gas away from these two stable phases, potentially explaining observationally inferred temperatures that depart from equilibrium expectations; we discuss these issues in § 5. It is, nevertheless, of significant interest to study in detail how TI develops nonlinearly to establish a two-phase cloudy medium in the absence of other potential effects such as localized heating, impacts from large-scale shocks, or stresses associated with MHD turbulence. Results of these carefully controlled pure TI simulations are valuable for characterizing the timescale to develop a two-phase medium, as well as its structural and kinetic properties. "Pure TI" models also represent a baseline for comparison of models incorporating more complex physics.

Once the particular form of the cooling curve has been chosen, the development of TI is primarily a function of four parameters: the cooling time, $t_{\rm cool}$, the heating time, $t_{\rm heat}$, the sound crossing time, $t_{\rm sound}$, and the conduction length scale, $\lambda_{\rm F}$. The cooling time depends on the specific cooling function; for the cooling curve we adopt (Sánchez-Salcedo et al. 2002), in varying temperature regimes we have

$$t_{\rm cool} = \frac{\mathcal{E}}{\rho^2 \Lambda} = \begin{cases} 1.2 \times 10^4 \text{ yr } \dfrac{(P/k)/2000}{(n/20)^2 (T/100 \text{ K})^{2.12}} & 10 < T < 141 \text{ K}, \\ 1.5 \times 10^4 \text{ yr } \dfrac{(P/k)/2000}{(n/10)^2 (T/200 \text{ K})^{1.00}} & 141 < T < 313 \text{ K}, \\ 3.7 \times 10^5 \text{ yr } \dfrac{(P/k)/2000}{(n/1)^2 (T/2000 \text{ K})^{0.56}} & 313 < T < 6102 \text{ K}, \\ 1.1 \times 10^6 \text{ yr } \dfrac{(P/k)/2000}{(n/0.25)^2 (T/8000 \text{ K})^{3.67}} & 6102 < T < 10^5 \text{ K}. \end{cases} \quad (5)$$

The heating time

$$t_{\rm heat} = \frac{\mathcal{E}}{\rho \Gamma} = 4.1 \times 10^5 \text{ yr} \frac{(P/k)/2000}{(n/1)} \quad (6)$$

for $\Gamma = 0.015$ ergs s $^{-1}$ g^{-1}. We can also define an effective cooling/heating time as $t_{\rm cool,\,eff} = |t_{\rm cool}^{-1} - t_{\rm heat}^{-1}|^{-1}$; at thermal equilibria, $t_{\rm cool,eff}$ becomes infinite. The sound crossing time over distance l is

$$t_{\rm sound} = \frac{l}{c_s} = 1.1 \times 10^6 \text{ yr} \frac{l/5 \text{ pc}}{(T/2000 \text{ K})^{1/2}} \quad (7)$$

In Figure 3, we plot $t_{\rm cool,\,eff}$, and $t_{\rm sound}$ for $l = 5$ pc as a function of density for $P/k = 2000$ K cm $^{-3}$. For a range of densities 0.1 cm$^{-3} < n < 1$ cm^{-3}, the sound crossing time is

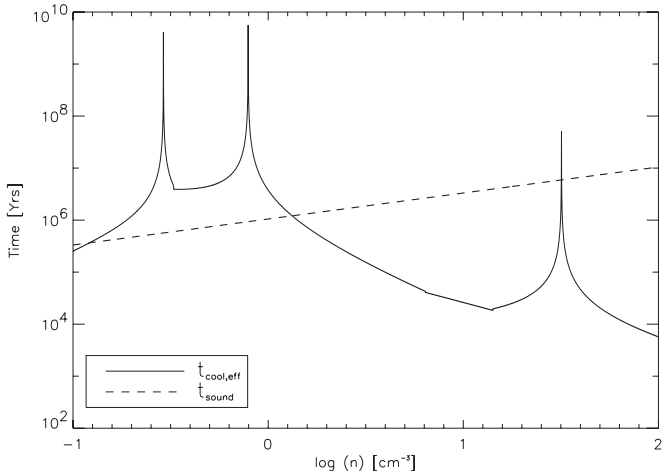

FIG. 3.—Comparison of $t_{\rm cool,\,eff}$ and $t_{\rm sound}$ as a function of density for $P/k = 2000$ and $l = 5$ pc. For a range of 0.1 cm$^{-3} \lesssim n \lesssim 1$ cm^{-3}, the sound crossing time is less than the effective cooling time, so that gas can evolve at approximately constant pressure. For higher densities, $t_{\rm cool,\,eff}$ is typically an order of magnitude shorter than $t_{\rm sound}$, and the gas tends to cool toward the equilibrium curve. The peaks where $t_{\rm cool,\,eff}$ approaches infinity represent the equilibrium densities ($n = 0.29$, 0.78, and 32 cm^{-3}) at which heating and cooling rates are equal for $P/k = 2000$.

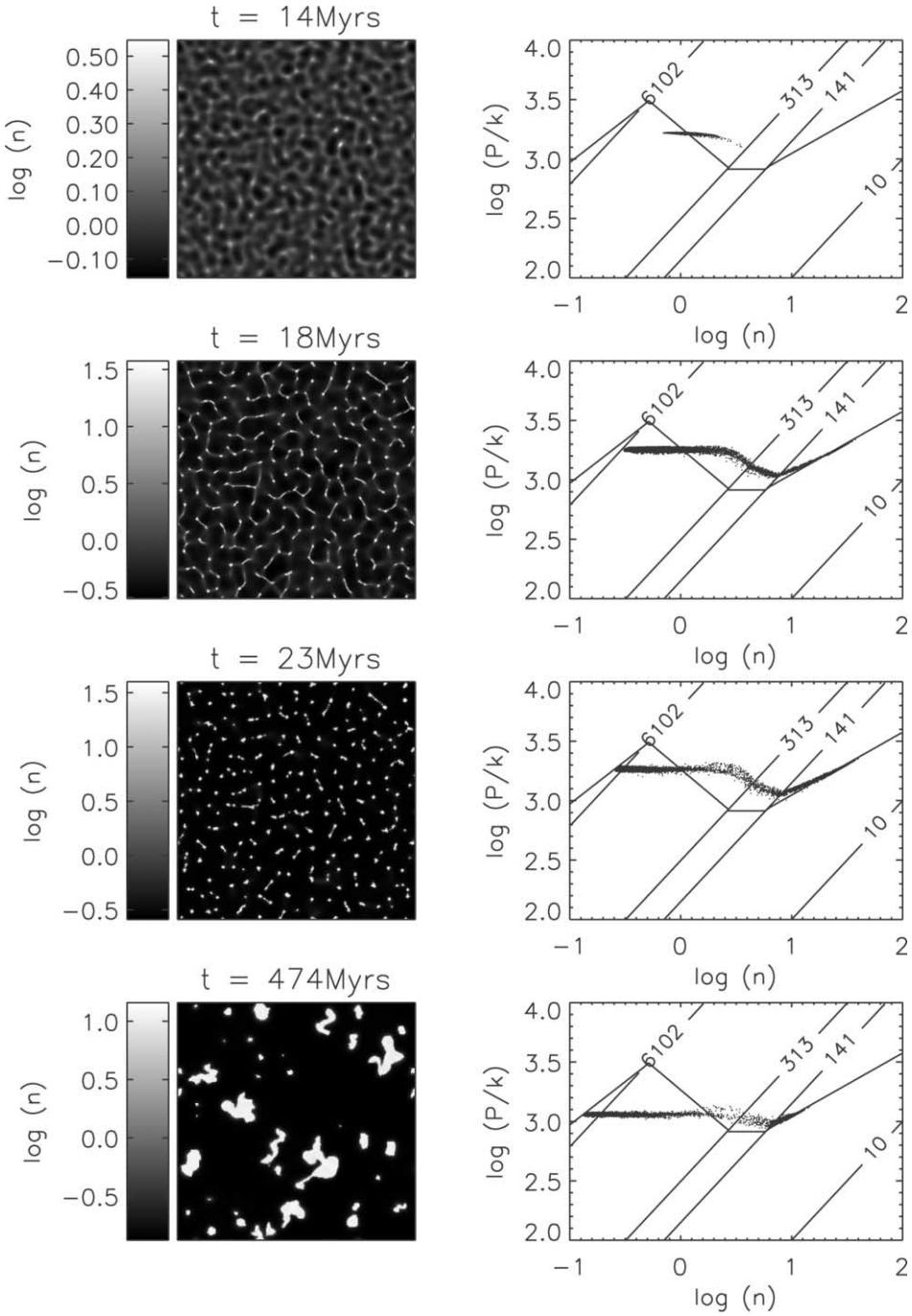

FIG. 4.—Density evolution in the TI simulation. *Left*: Snapshots of $\log n$ at representative times as noted. *Right*: Scatter plots of n and P/k from the simulation, together with the equilibrium cooling curve and the labeled temperature contours that demark the transitions between the F, G, and H phases. [*This figure is also available as a color mpeg animation in the electronic edition of the Astrophysical Journal.*]

significantly shorter than the effective cooling time; otherwise $t_{\rm sound}$ is typically more than an order of magnitude longer than $t_{\rm cool,\,eff}$.

To simulate TI under conditions representative of the general diffuse ISM, we adopt an initial density of $n = 1$ cm^{-3} and set the initial pressure to $P/k = 2000$ K cm $^{-3}$; all velocities are initially set to zero. Random pressure perturbations with an amplitude less than 0.1% are added to seed the TI. The gas is initially in a weakly cooling state, since the equilibrium pressure corresponding to $n = 1$ cm^{-3} is $P/k = 1660$ K cm $^{-3}$. The simulation proceeds for 470 Myr, corresponding to two galactocentric orbits at the solar circle.

3.2. *Structural Evolution*

The initial development of TI proceeds quickly. In Figure 4 we show four snapshots at different times of the density distribution alongside scatter plots of pressure versus density overlaid on the equilibrium cooling curve. Structure begins to form at about 5 Myr, and density contrasts continue to increase at constant pressure until 14 Myr as shown in Figure 4. The Fourier transform of the density distribution at this time, Figure 5, shows that the majority of the power is concentrated at $(k_x^2 + k_z^2)^{-1/2} \equiv k = 14$. Allowing for geometrical factors, this is consistent with the one-dimensional linear theory pre-

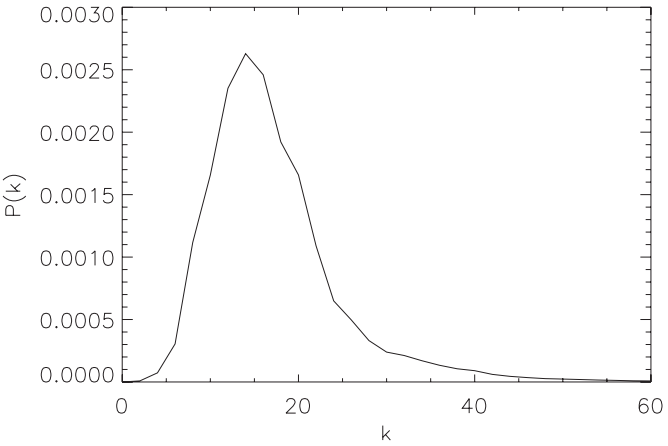

FIG. 5.—Power spectrum of the TI density distribution at 14 Myr

diction that the most unstable wavelength is $k \sim 9$ for our chosen value of conduction. A network of filaments briefly forms at about 18 Myr connecting the regions of highest density, with flow moving along the filaments increasing the number density to as high as 18 cm^{-3}. By 23 Myr the dense gas has collected in condensations and has relaxed to approximate thermal equilibrium. The size scale of the cold clumps is initially only a few parsecs and is relatively uniform. However, random motions of the newly formed clouds leads to merging and disassociation; conductive evaporation at its boundaries can also alter the shape of a clump. By the end of the simulation, at 474 Myr, the typical cloud size has increased significantly to $\sim$10 pc; however, a number of smaller clouds either remain from the initial TI development or have formed as a result of disassociation.

In Figures 6*a*–6*c*, we plot the volume-weighted and mass-weighted density PDFs for the first three snapshots from Figure 4. At $t = 14$ Myr, in Figure 6*a*, all of the gas is in the unstable range. Already, however, in Figure 6*b*, after 18 Myr, the distribution has begun to separate into two distinct phases. At $t = 18$ Myr, 69%, 28%, and 3% of the gas by volume is in the F (warm), G (unstable), and H (cold) phases, respectively, which are defined by our cooling curve as the ranges $n < 0.5$ cm^{-3}, 0.5 cm^{-3} $< n <$ 5.8 cm^{-3}, and 5.8 cm^{-3} $< n$, respectively. By mass these proportions are reversed to 29%, 23%, and 49%. From about 100 Myr through the end of the simulation, the distribution of cloud sizes evolves, but the PDF remains relatively unchanged, with 12%, 2%, and 86% of the mass residing in the F, G, and H phases, respectively

We also performed the same simulation but increased the resolution to 512^2. The conduction coefficient is not changed, so $n_c = 16$. We find similar results overall. In particular, the mass-weighted density PDFs are compared in Figure 6*d*. These PDFs exhibit no significant differences, confirming the robustness of our results.

3.3. *Thermal Evolution*

Alongside the images of density in Figure 4 we show scatter plots of n against P for all zones in the grid at the same times. In the initial state, pressure is constant, and $t_{\rm sound}$ at 5 pc ($\sim\frac{1}{2}$ the length of the fastest growing TI mode) is shorter than $t_{\rm cool}$ (see Fig. 3). Toward the low-density warm phase, $t_{\rm sound} \ll t_{\rm cool}$, and gas parcels in regions undergoing rarefaction are able to heat nearly isobarically. Thus, all zones at densities lower than the

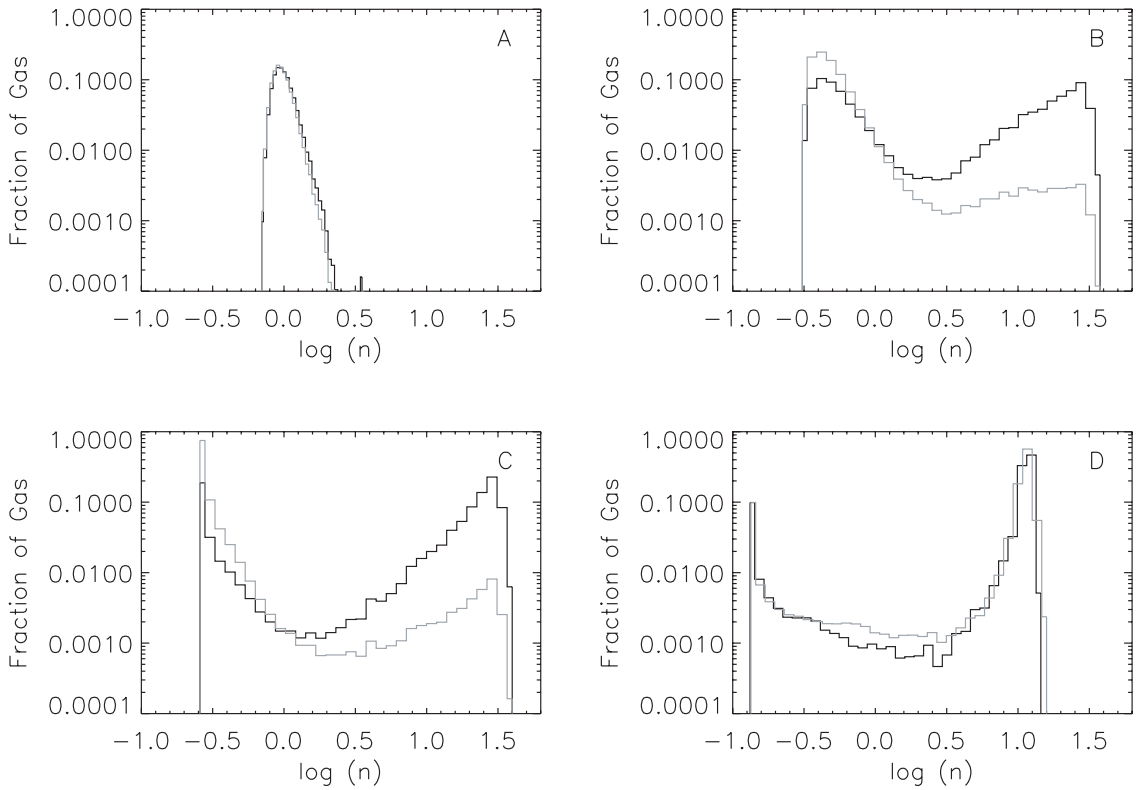

FIG. 6.— (*a*–*c*) Mass (*black line*) and volume (*gray line*) density PDFs for TI at the same times as the first three snapshots in Fig. 4. (*d*) Comparison of the mass-weighted density PDF for the standard resolution of 256^2 (*black line*) and 512^2 (*gray line*) at time 474 Myr.

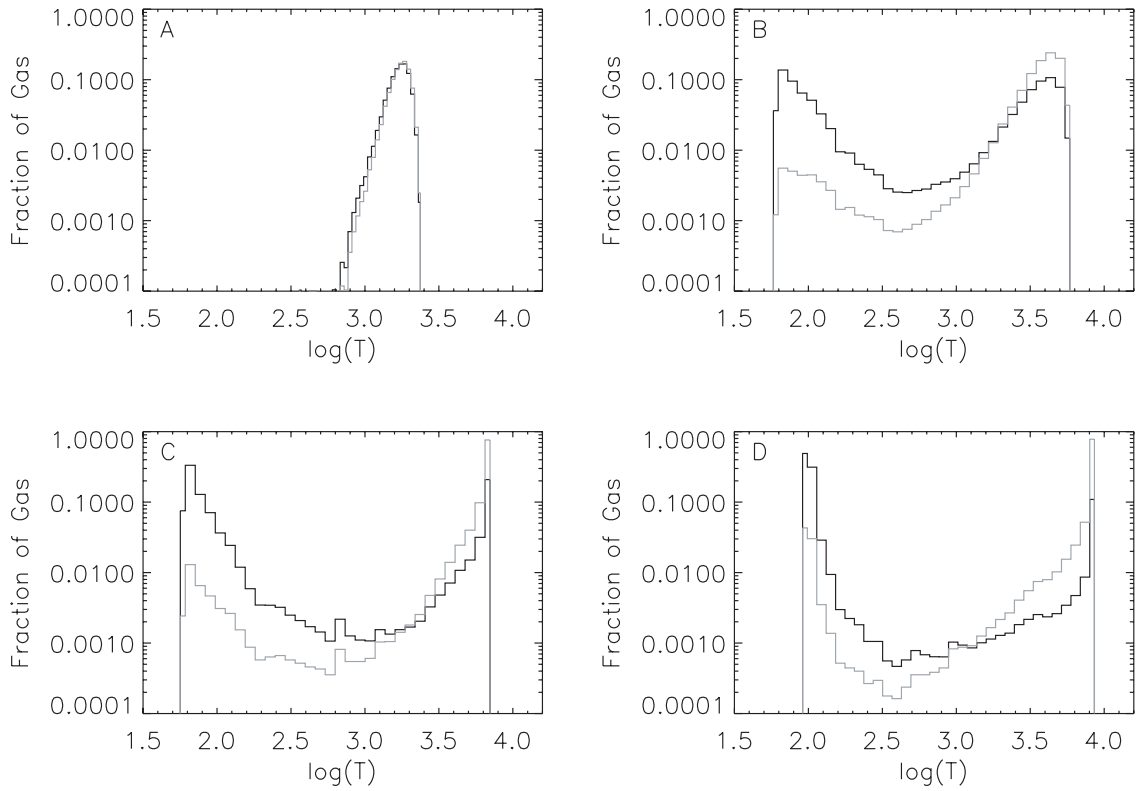

FIG. 7.—Mass (*black line*) and volume (*gray line*) temperature PDFs for the snapshots in Fig. 4 (time increases from A to D)

mean are filled with an intercloud medium that maintains spatially nearly uniform pressure. For gas parcels undergoing compression and net cooling, as $\delta\rho$ becomes large, $t_{\rm cool} \ll t_{\rm sound}$, so the gas tends to cool toward the thermal equilibrium curve at a faster rate than the flow is able to readjust dynamically. After gas parcels reach near thermal equilibrium in the cold phase, they continue to be compressed until pressure equilibrium with the warm medium is reestablished. Over time, the average pressure in the simulation box decreases as a result of radiation from the cold phase.

Because the scatter plots in Figure 4 contain a large number of points, many fall in the unstable range, although the actual amount of material there is small. To quantify this, in Figure 7 we plot mass-weighted and volume-weighted temperature PDFs at times corresponding to the snapshots in Figure 4. As with the density PDF, the distribution is separated into two distinct phases in Figure 7*b* at 18 Myr and remains so for the duration of the simulation.

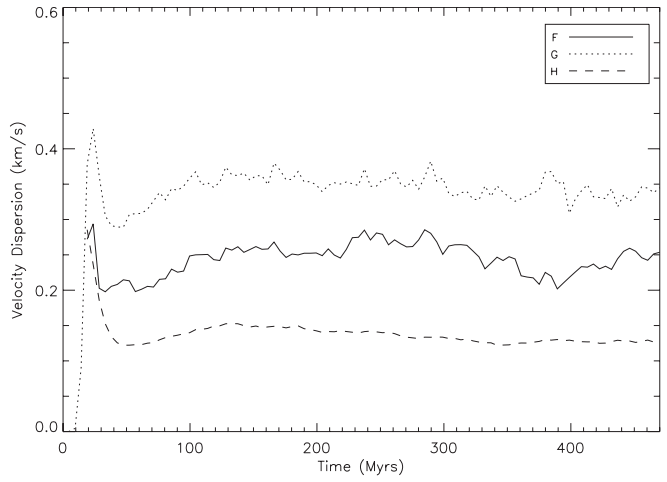

FIG. 8.—Evolution of velocity dispersion is $(v_x^2 + v_z^2)^{1/2}$ in the TI model. Typical velocities for the F (warm), G (unstable), and H (cold) phases are 0.25, 0.35, and 0.15 km s^{-1}, respectively.

3.4. *Kinetic Evolution*

TI is a dynamic process, and a number of recent works have proposed that TI may help contribute to exciting turbulence in the ISM. In Figure 8 we plot the mass-weighted velocity dispersions for gas in the F, G, and H phases separately. For all phases, the largest velocities occur during the condensation stage at early times (10–20 Myr), corresponding to about 5 times the *e*-folding time of the dominant linear instability. The peak velocity is about 0.45 km s^{-1} for the unstable (G) phase and is $\sim$0.3 km s^{-1} for the two stable phases. At later times the velocity dispersion in each phase remains relatively constant, with the largest value (0.35 km s^{-1}) for phase G, next largest (0.25 km s^{-1}) for the warm phase, F, and smallest (0.15 km s^{-1}) for the cold phase, H. The standard deviation of the total velocity dispersion is typically 0.15 km s^{-1}. For comparison, typical sound speeds of the F, G, and H phases are 7–8, 1–5, and 0.6–1 km s^{-1}, respectively. Thus, the mean turbulent velocities are all subsonic.

4. MRI SIMULATIONS

4.1. *MRI Physics*

In a series of four papers, Balbus & Hawley presented the first linear analysis and numerical simulations of MRI in the context of an astrophysical disk (Balbus & Hawley 1991, 1992; Hawley & Balbus 1991, 1992). The physical basis for

the instability is relatively simple, and there are two requirements for the instability to be present: a differentially rotating system with decreasing angular velocity as one moves outward through the disk and a weak magnetic field (strong magnetic fields have a stabilizing effect). As fluid elements are displaced outward (inward) the magnetic field resists shear and tries to keep the fluid moving at its original velocity. Because of these magnetic stresses, fluid elements gain (lose) angular momentum, the centrifugal force becomes too large (small) to maintain equilibrium at the new position, and the fluid element moves farther outward (inward). This leads to the transport of angular momentum outward through the disk.

For a complete linear analysis of the MRI in two dimensions, we refer the reader to Balbus & Hawley (1991). Here we simply summarize the important formulae for axisymmetric modes with wavenumber $\boldsymbol{k} = k_z\hat{z}$ and $\boldsymbol{B}_0 = B_0\hat{z}$. The growth rates are given by

$$\frac{\gamma^2}{\Omega^2} = \nu^2\left\{\frac{2q-\nu^2}{\nu^2+2-q+[4\nu^2+(2-q)^2]^{1/2}}\right\}, \qquad (8)$$

where $\nu \equiv k_z v_{Az}/\Omega$ in terms of the Alfvén speed $v_{Az} \equiv B_{0z}(4\pi\rho)^{-1/2}$. The maximum growth rate occurs when

$$\left(\frac{kv_{Az}}{\Omega}\right)_{\rm peak} = \frac{\left[4-(2-q)^2\right]^{1/2}}{2}, \qquad (9)$$

i.e., $\lambda_{\rm peak} = 4\pi v_{Az}/(\sqrt{3}\Omega)$ for $q = 1$; here the growth rate is $\gamma_{\rm peak} = \Omega q/2 \rightarrow \Omega/2$. The highest wavenumber for which axisymmetric MRI exists when $\boldsymbol{B}_0 = B_0\hat{z}$ is

$$\left(\frac{kv_{Az}}{\Omega}\right)_{\rm max} = \sqrt{2q}. \qquad (10)$$

We have tested the code without cooling and conduction and found that it can accurately reproduce the predicted linear growth rates of the MRI. We do not detail the results here; instead we refer the reader to Hawley & Balbus (1992) for a complete analysis of similar models.

Based on the linear dispersion relation, for sufficiently weak magnetic fields, modes with a range of k_z (and also k_r) may grow. The smallest permissible wavenumber for a simulation is $(k_z)_{\rm min} = 2\pi/L_z$, where L_z is the vertical dimension of the computational box. At late times in two-dimensional axisymmetric simulations (Hawley & Balbus 1992), MRI becomes dominated by a "channel" solution corresponding to the smallest permissible vertical wavenumber, i.e., with flow moving toward the inner regions of the disk on one (vertical) half of the grid, and flow moving toward the outer regions in the other (vertical) half of the grid. This pure "channel flow" is unphysical; for a three-dimensional system it is subject to nonaxisymmetric parasitic instabilities (Goodman & Xu 1994). In three-dimensional nonaxisymmetric simulations (e.g., Hawley et al. 1995) the channel solution forms at early times but later develops into a fully turbulent flow.

The MRI has primarily been studied in the context of accretion disks but can be important in any differentially rotating disk system provided the magnetic fields are not too strong. In addition to axisymmetric modes, nonaxisymmetric MRI modes can also grow directly (see, e.g., Balbus & Hawley 1992 and Kim & Ostriker 2000, eqs. [80] and [81] for instantaneous growth rates and instability threshold criteria in various limits). The axisymmetric mode with wavelength $\lambda_z \sim 2H$ is the most difficult to stabilize as B_z increases; from equation (10), taking $\Omega = 26$ km s^{-1} kpc^{-1}, $q = 1$, a disk scale height $H = 150$ pc, and a uniform density $n = 0.6$ cm^{-3}, MRI will be present provided $B_z < 0.6$ μG. For the Milky Way, this is consistent with the observed solar neighborhood estimate $|B_z| = 0.37$ μG (Han, Manchester, & Qiao 1999). If a multiphase system behaves similarly to the corresponding uniform-density medium, then we may expect MRI to be important in the Galactic ISM. Here we explore how MRI development can be affected by strong nonuniformity in the density structure.

4.2. *Evolutionary Development: TI+MRI Model*

To study nonlinear development of the MRI in a nonuniform medium, we first perform a simulation identical to the TI model run described in § 3 but now include magnetic fields and sheared rotation. All hydrodynamic variables are initialized as described in § 3. The magnetic field is vertical with $\beta = P_{\rm gas}/P_{\rm mag} = 1000$. The rotation rate is set to 26 km s^{-1} kpc^{-1}, representative of the local value near the Sun, and we set the shear parameter $q = 1.0$ to describe a flat rotation curve. With these parameters, from equation (10), the smallest-scale uniform-density MRI mode that would fit within our $L_z = 100$ pc box has $k_z = 3$ (in units of $2\pi/L_z$).

On the left in Figure 9 we show snapshots of number density overlaid with magnetic field lines at three representative times, and on the right we show the corresponding mass-weighted density PDF. The timescale for development of the MRI is much longer than that of TI, so that the initial development is essentially the same as in the purely hydrodynamic case. During the TI condensation phase, the magnetic field becomes kinked as the filaments condense into small clouds. The remaining random motions of the clouds leads to further distortion of the magnetic field, as can been seen at 237 Myr. The channel solution has clearly taken hold by 474 Myr, and the $k_z = 1$ mode (in units of $2\pi/L_z$) dominates.

Similarly to our analysis of kinetic evolution for the TI model, in Figure 10 we plot the velocity dispersion for the F, G, and H phases as a function of time in the TI+MRI model. Initially, these are similar to the hydrodynamic case, with all velocities less than 0.5 km s^{-1}. As the channel solution develops, the velocity dispersion begins to increase at about 500 Myr and peaks at the end of the simulation in phase F at approximately 1.5 km s^{-1} . The peak velocity dispersion is about 1.2 km s^{-1} for phase G and 0.9 km s^{-1} (approximately the sound speed) for phase H, all toward the end of the simulation.

As in the hydrodynamic model, the PDFs for the TI+MRI model are clearly two-phase, with small amounts of gas contained in the unstable regime. At very late times the fully developed channel solution tends to increase the proportion of unstable gas. In Figure 11 we plot the mass-weighted temperature PDF of the TI+MRI model 800 Myr, and the same quantity for the TI run at 474 Myr. We do not expect that the PDF for the TI run would evolve significantly if the simulation had been continued to 800 Myr. Evidently, the dynamical flows induced by the MRI can significantly affect the temperature distribution. The larger velocity dispersion and kinked magnetic fields due to the channel solution can compress portions of cold clouds, decreasing the temperature

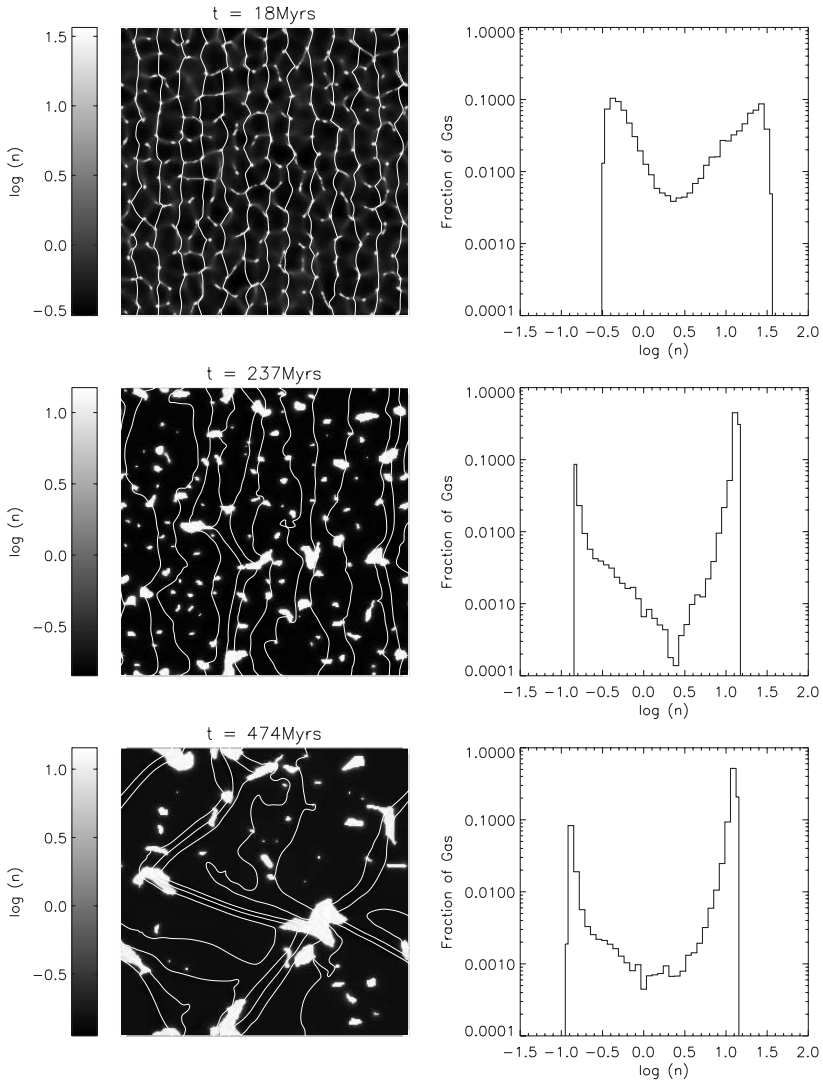

FIG. 9.—Structural evolution of the TI+MRI simulation. *Left*: Snapshots of $\log n$ at representative times as noted, overlaid with magnetic field lines. *Right*: Mass-weighted density PDF at the same times as the snapshots. [*This figure is also available as a color mpeg animation in the electronic edition of the Astrophysical Journal.*]

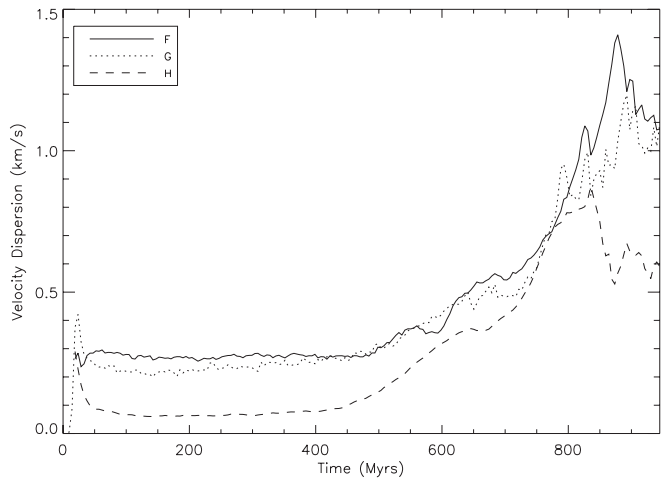

FIG. 10.—Mass-weighted velocity dispersion is $(v_x^2 + v_z^2)^{1/2}$ for TI+MRI model, separated by phase. The initial velocity dispersion is due to the development of TI (see Fig. 8). After 400 Myr the MRI becomes important, and the channel solution increases the velocity dispersion to as high as 1.4 km s^{-1} toward the end of the simulation.

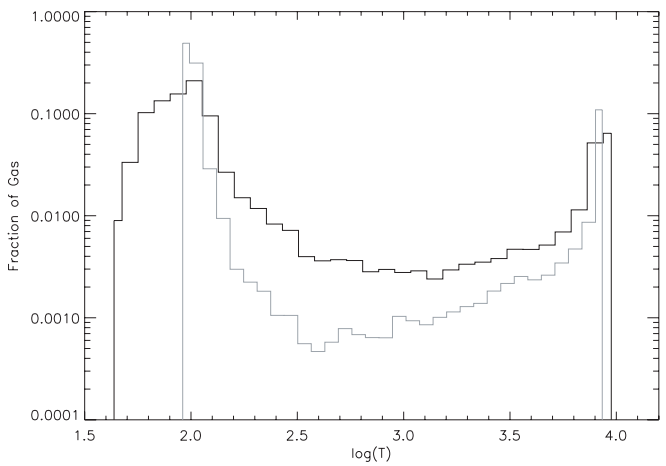

FIG. 11.—Mass-weighted temperature PDF for the TI run at 474 Myr (*gray line*) and TI+MRI at 800 Myr (*black line*), after the channel solution has fully developed. The active dynamics of MRI leads to the presence of high-density/low-temperature gas.

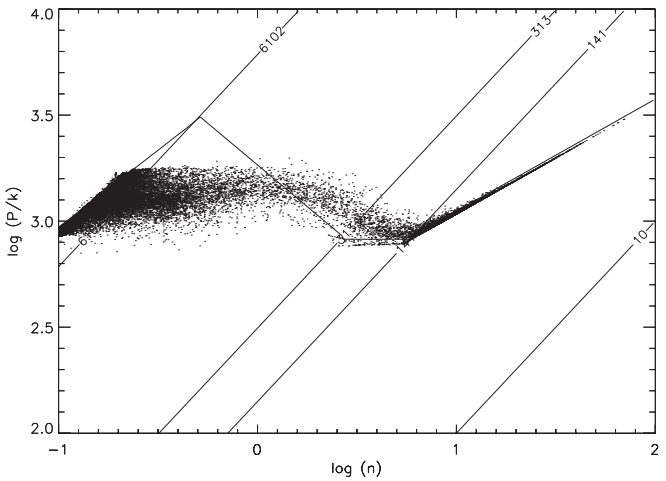

FIG. 12.—Scatter plot of n and P/k at 800 Myr, near the end of the simulation, for the TI+MRI model. Cooling timescales are short for the high-density gas, so gas remains near thermal equilibrium for a range of pressures. In the low-density regime, cooling timescales are longer, and there can be significant departures from thermal equilibrium.

correspondingly. Although still dominated by distinct warm and cold phases, there is also a higher proportion of gas in the unstable regime. For the same model snapshot, Figure 12 shows a P/k versus n scatter plot, overlaid on the equilibrium cooling curve. In the high-density regime, cooling times are short, and the gas is not far from equilibrium. At low densities cooling times are longer, and gas can be found out of thermal equilibrium.

Since the two-dimensional channel solution would break up in a real three-dimensional disk because of parasitic instabilities (Goodman & Xu 1994), we do not expect the late-time effects seen in our models to have direct implications for the temperature distribution in the diffuse ISM. They illustrate, however, the more generic point that spatially varying rotational shear coupled to magnetic fields can create stresses that force gas away from the stable equilibrium phases. We discuss this further, highlighting differences that might be expected for three-dimensional MRI, in § 5.

Important questions for assessing MRI development in a cloudy medium are how the spatial scales and timescales of

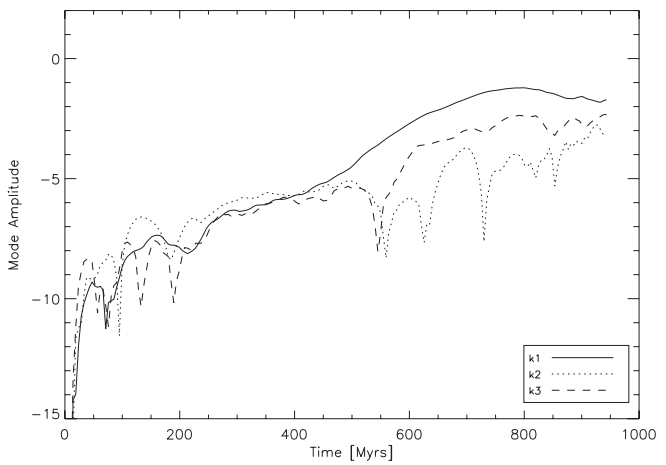

FIG. 13.—Mode amplitudes for B_y in the TI+MRI model. For the first 500 Myr the $k = 1$, 2, and 3 modes are approximately equal in amplitude, but the $k = 1$ mode is dominant after this point.

the fastest growing modes differ, compared to those in single-phase counterpart systems. We measure MRI mode amplitudes in the simulations by taking the Fourier transform of B_y as a function of time, from which we can calculate the growth rates. The $k = 1$, 2, and 3 mode amplitudes are plotted in Figure 13. There is not an obvious linear stage from which we can measure the growth rate, but between 284 and 470 Myr the average $k = 1$ growth rate is about 0.28 Ω, compared to the predicted rate of 0.34 Ω at the average density of the model. At the average density, linear theory predicts that the most unstable mode is at $k = 2$, with a growth rate of 0.50 Ω, and the $k = 3$ mode is unstable as well, with a predicted growth rate of 0.41 Ω. Between 284 and 470 Myr we measure a mean growth rate for the $k = 2$ and 3 modes to be 0.12 and 0.18 Ω, respectively. At the density of the warm medium, only the $k = 1$ mode is predicted to be unstable in our simulations, with a growth rate of 0.45 Ω. Thus, growth rates of available modes appear somewhat lower than they would be for a medium at either the mean density or the density of the warm medium. In addition, initial growth does not show the clear dominance of a single fastest growing mode that is evident in comparison with adiabatic test simulations for a single-phase medium. However, at late times, the $k = 1$ mode grows to exceed the other low-order modes, similarly to the findings of Hawley & Balbus (1992) for a single-phase medium.

4.3. *Evolutionary Development: Cloud+MRI Model*

Because the initial MRI growth in the previous model may be strongly affected by lingering dynamical effects of TI, it is of interest to consider MRI development in a medium that contains two distinct phases from the outset. In our next simulation we therefore begin with a two-phase medium in approximate equilibrium, rather than developing a two-phase medium from thermally unstable gas. We embed 59 high-density clouds in a low-density ambient medium such that the average density is the same as that of previous TI simulations. To set up the initial conditions allowing for conduction at cloud/intercloud interfaces, we first create "template" cloud profiles by embedding a single high-density cold cloud in a low-density warm medium and evolving until a thermally and dynamically relaxed state is reached. This profile (density, pressure, and velocity) is then copied to randomly chosen locations on the grid, with the condition that cloud centers must be at least 20 zones apart. We initialize the magnetic field after this "cloud embedding" procedure. The simulation is then evolved as the MRI develops.

In Figure 14 we show three snapshots from the "cloud+MRI" simulation, along with mass-weighted density PDFs. The MRI takes about 500 Myr until its development begins to become apparent, as can be seen in the poloidal field lines at 464 Myr in Figure 14. At 701 Myr, many of the clouds have merged and have significant velocities as the MRI channel solution begins to take hold. Initially, the mass-weighted density PDF shows almost no gas in the unstable range, but as the MRI begins to develop, this phase begins to become populated, and the PDF becomes very similar to those from the TI+MRI simulations.

Perhaps the most interesting results from this "cloud+MRI" simulation are the behavior of the mode amplitudes and growth rates. Initially, the clouds contain negligible velocities and are in what would be a steady state if magnetic fields were not present. We might expect, then, to find "cleaner" MRI growth rates than those for the TI+MRI runs. The mode

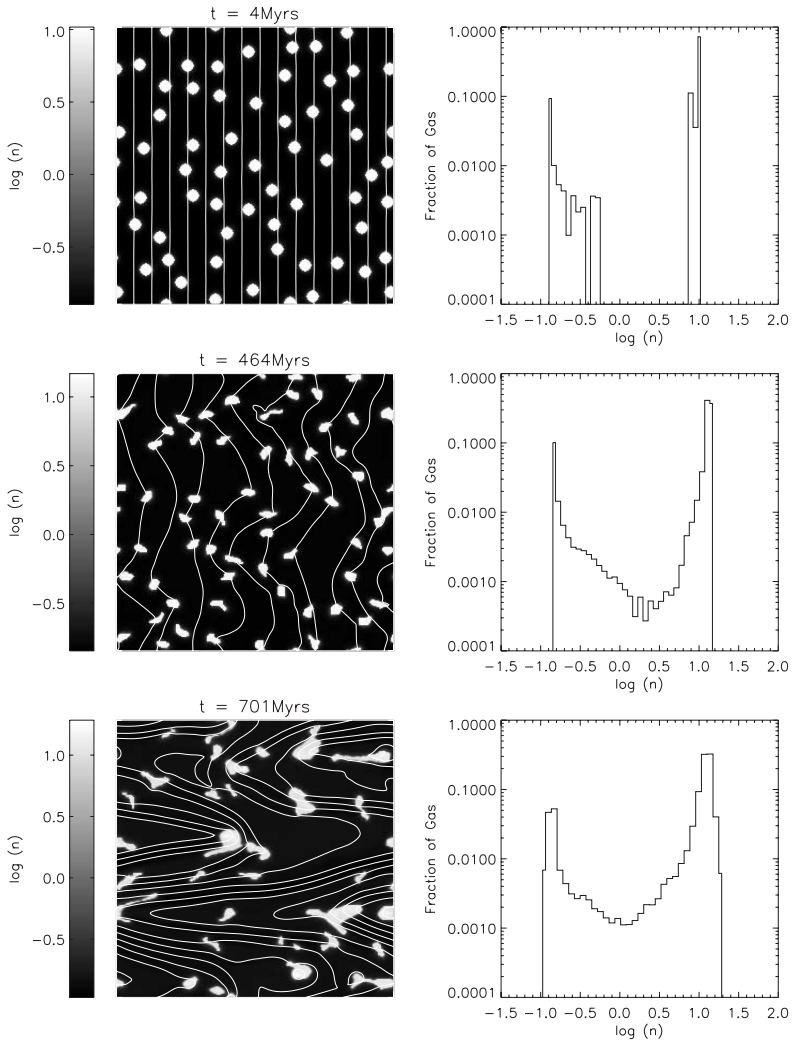

FIG. 14.—Structural evolution of cloud+MRI simulation. *Left*: Snapshots of $\log n$ at representative times as noted, overlaid with magnetic field lines. *Right*: Mass-weighted density PDF at the same times as the snapshots. [*See the electronic edition of the Journal for a color version of this figure.*]

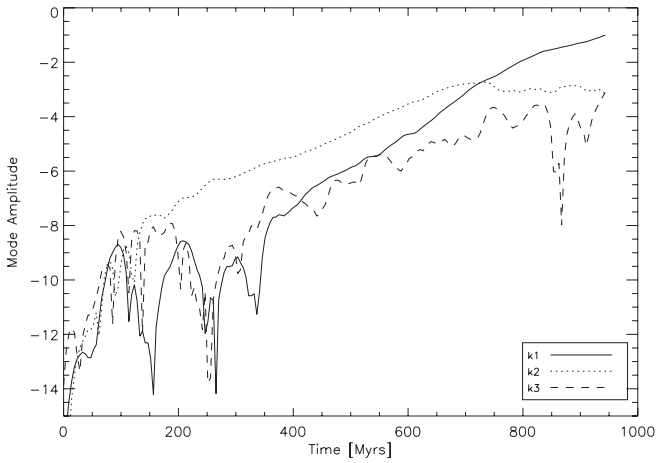

FIG. 15.—Mode amplitudes of B_y in the cloud+MRI simulation. The $k = 2$ mode is initially the largest, but by the end of the simulation the $k = 1$ mode has become dominant.

amplitudes for $k = 1$, 2, and 3 are plotted in Figure 15. Initially, the $k = 2$ mode is dominant and shows approximate exponential growth between 300 and 700 Myr, with an average growth rate of 0.34 Ω, compared to the predicted rate 0.50 Ω at the average density. The $k = 1$ mode also shows approximate linear growth with an average rate of 0.47 Ω measured from 450 to 900 Myr and becomes the dominant mode at around 800 Myr. At the density of the warm medium, the theoretical growth rate of the $k = 1$ mode is 0.45 Ω, and at the average density it is 0.34 Ω. The $k = 3$ growth rate, measured between 400 and 800 Myr is 0.33 Ω, which we can compare to the predicted value at the average density of 0.41 Ω. Thus, similarly to the TI+MRI model, growth rates are slightly lower than they would be in a medium with the same mean density. There is, however, a longer period of dominance by the mode with the fastest expected growth rate.

For comparison, we also performed an MRI simulation with cooling and conduction disabled, initially at uniform density and seeded with the velocity and pressure profiles from the initial state of the previous "cloud+MRI" simulation; we also performed zero-conduction, zero-cooling test simulations seeded with random perturbations. The growth rates are in reasonable agreement between these simulations, although the case directly seeded with random perturbations had cleaner

growth of mode amplitudes. Most importantly, we find that rather than $k = 2$ predominating, as we found in the "cloud+MRI" simulation, the $k = 3$ mode in the single-phase comparison model is dominant until late times. This suggests that the initial perturbations are strongest at $k = 3$, but the presence of the multiphase medium in the "cloud+MRI" model significantly inhibits the growth of this mode because the inertial load varies strongly over a wavelength for $k = 3$.

4.4. *Perspective: Effects of Cloudy Structure*

There are a number of ways MRI growth rates and preferred scales could be affected by the influence of a cloudy background density structure, and signs of these effects are evident in our simulations. First, both growth rates and preferred scales are dependent on the Alfvén speed, which is a function of density. The cold, dense clouds will be MRI-unstable at small scales compared to the larger preferred scales of the warm, low-density, ambient medium. For fixed magnetic field strength, MRI wavelengths are inversely proportional to density. Thus, MRI wavelengths in cold, dense gas will be a few parsecs, while MRI wavelengths in warm, diffuse gas will be several tens of parsecs. Although the MRI wavelengths in dense gas may be smaller than individual cold clouds, permitting initial rapid growth, further development of the small-scale instability is limited by clouds' small radial extent. Long-term MRI development must therefore have characteristic wavelengths representative of either the average density conditions or the pervasive low-density warm, intercloud gas. This expectation is indeed consistent with our results. As seen in Figures 9 and 14, both the diffuse gas and the cold clouds participate together in an overall large-scale flow. The cold clouds are frequently the sites of strong kinks in the magnetic field.

One might also expect the preferred scales for MRI to be affected by cloud spacing. If cloud spacing is small compared to a given wavelength, then the MRI growth rate might be expected to be similar to that under average density conditions. Thus, if the fastest growing wavelength at the mean density is large compared to cloud spacing along a field line, then this might be expected to be the dominant wavelength. This situation is indeed evident in the second panel (464 Myr) of Figure 14, in which the $k = 2$ mode dominates, even though, as described above, the input perturbation spectrum is such that the $k = 3$ mode would dominate if the density were uniform. On the other hand, if fewer, more massive clouds exist, cloud separations will be larger, which could suppress MRI growth at wavelengths shorter than cloud spacings and encourage MRI development on the largest scales. Evidence of this effect can be seen in the third panel (474 Myr) of Figure 9.

Finally, if total mass is distributed very unevenly with magnetic flux, then MRI may develop more rapidly and at longer wavelengths in regions where there is a comparatively low inertial load. In simulations (not shown) we have performed that have alternating radial zones of high and low mass loading on field lines (initiated with cold clouds at intersections in a Cartesian grid), we indeed see this effect. Development of MRI in the low-inertia "pure warm" phase is, however, checked when the radially moving flow collides with the high-inertia cold clouds.

To test whether the growth rate of the smaller scale $k = 2$ mode (essentially near the lower wavelength limit for behavior as at a single average density) could be enhanced in TI+MRI models, we also performed an additional random TI simulations in which a $k = 2$ perturbation was added shortly after the initial condensation phase. The perturbation was added at about the 20% level in v_1. For the first 500 Myr, the $k = 2$ mode is strongest with a growth rate of 0.36 Ω. After 500 Myr the $k = 1$ mode, with a growth rate of 0.47 Ω, is again dominant.

Taken together, the simulations of this section show that the development of the MRI in the presence of a cloudy medium has modest differences compared to the corresponding development in a single phase medium at the average density. The dominant wavelengths are similar to those predicted by linear theory at mean-density conditions, and growth rates are also similar but slightly smaller. The spacings between clouds affects which among the low-k modes dominates the power during the exponential-growth phase. At very late times the $k_z = 1$ mode is dominant in all simulations, consistent with the ultimate dominance of this channel flow in the single-phase models of Hawley & Balbus (1992).

5. SUMMARY AND DISCUSSION

Thermal and magnetorotational instabilities may play a major role in determining the physical properties of the diffuse ISM. In regions far from active star formation or a recent supernova explosion, TI and MRI may even be the primary processes driving structure and dynamics in the ISM on scales $\lesssim 100$ pc. The PDFs of gas density and temperature, the characteristic sizes, shapes, and spatial distributions of cloudy structures, and the amplitudes and spectral properties of turbulent velocities and magnetic fields may all be strongly influenced by TI and MRI. In addition, development and saturation of TI and MRI may be strongly interdependent. In this paper, we have initiated a study of these important processes using numerical MHD simulations. The current work focuses on code tests and two-dimensional models using a microphysics implementation appropriate for the atomic ISM. In addition to characterizing the properties of TI and MRI modes in their nonlinear stages, this study lays the groundwork for future three-dimensional simulations that will be used to investigate quasi-steady turbulence.

In the following, we summarize the results presented herein, compare to other recent work, and discuss key issues for future investigation:

1. *Numerical methods*.—We have implemented atomic-ISM heating/cooling and thermal-conduction source terms in the energy equation of the ZEUS code (using implicit and explicit updates, respectively). For conditions representing the mean pressure and density in the ISM, we find excellent numerical agreement with the analytic growth rates of thermally unstable modes for a large range of wavelengths and thermal conductivity coefficients. On the basis of these tests and confirmation of acceptable results for advection of high-contrast contact discontinuities (warm/cold pressure equilibrium interfaces) on the grid, we adopt a value of $\mathcal{K} = 10^7$ ergs cm^{-1} s^{-1} K^{-1} such that the Field length is resolved by 8 (16) zones in (100 pc)^2 simulations with 256^2 (512^2) cells.

Explicit inclusion of conduction is important for suppressing numerically unresolved TI-driven amplification of grid-scale noise; Koyama & Inutsuka (2003) have also recently highlighted the importance of implementing conduction for simulations of thermally bistable media. In some previous simulations of TI (Kritsuk & Norman 2002a, 2002b) under strongly cooling conditions, conduction was not included; since those simulations began with relatively large-amplitude

(5%) perturbations on resolved scales, however, subdominant effects from unresolved growth at grid scales in the initial stages of TI would be less noticeable. In other recent work (Vázquez-Semadeni et al. 2003) simulations of TI using spectral algorithms (with explicit diffusive terms in the equations of motions) appear to have difficulty reproducing the analytic growth rates in some circumstances. Conceivably, this may be a sign of numerical diffusion that could tend to produce more gas in thermally unstable regimes than is realistic, in simulations using these computational methods.

2. *Nonlinear development of TI.*—In "pure TI" simulations, in which we initialize gas at $P/k = 2000$ K cm^{-3} and $n = 1$ cm^{-3} in a (100 pc)^2 box with 0.1% initial pressure perturbations, we find that TI develops at a characteristic length scale consistent with the predicted fastest growing mode, $\sim$12 pc for our adopted value of $\mathcal{K}$. As seen in other two-dimensional simulations (e.g., Vázquez-Semadeni et al. 2000), the structure initially resembles a "honeycomb" network of cells, and as nonlinear development proceeds, gas condenses into cold, compact clouds at the intersections of filaments. Gas undergoing rarefaction toward the warm phase heats nearly isobarically, because the sound crossing time is short compared to the net heating-cooling time. Gas undergoing compression toward the cold phase initially has isobaric evolution (while density perturbations remain low-amplitude), but then tends first to cool toward the equilibrium curve very rapidly (with an attendant pressure drop), and then dynamically readjusts its density and temperature until the pressure again matches ambient conditions. The time to establish a distinct two-phase structure of well-separated cold clouds within a warm ambient medium (see third panel of Fig. 4) is $\sim$20 Myr, or about 10 *e*-folding times in terms of the linear growth rate. In the subsequent evolution, the cold, dense clouds undergo successive mergers to produce larger structures.

The transition from nearly isobaric to more "isochoric"-like evolution for cold gas during nonlinear stages of condensation was recently emphasized by Burkert & Lin (2000), and snapshots of phase diagrams in Kritsuk & Norman (2002a) show a similar dip in pressure for overdense gas as it cools toward thermal equilibrium. Vázquez-Semadeni et al. (2003) found, similar to our results, that initial perturbations of similar or larger sizes to our dominant TI wavelength require times greater than 10 Myr to complete the condensation process, even when a much larger (10%) initial perturbations are used. The real level of conduction in the atomic ISM may be lower than the value we adopted (for numerical efficacy), with the fastest growing TI wavelength a factor of $\sim$4 smaller than our 12 pc value and the condensation time correspondingly shorter; Sánchez-Salcedo et al. (2002) found that 3 pc scale overdensities condense into clouds within 4 Myr. As the turbulent cascade is likely to maintain nonlinear-amplitude entropy perturbations down to subparsec scales, we expect that the fastest growing wavelength[3] is likely to dominate when TI occurs under "natural" circumstances, with later mergers producing larger clouds (see also Sánchez-Salcedo et al. (2002)).

3. *Gas phase distributions from TI.*—The bimodal density and temperature PDFs in our TI simulations mirror the distinct two-phase structure evident in late-time snapshots. Typical late-time warm-, cold-, and intermediate-temperature mass fractions are 12, 86, and 2%. For a two-phase medium with mean density $\bar{n}$ and cold and warm densities n_c and n_w, the fraction of mass in the cold medium is $f_c = (1 - n_w/\bar{n})(1 - n_w/n_c)^{-1}$. Provided $n_c \gg n_w$, the mass fraction in the warm medium is thus $f_w \approx n_w/\bar{n}$. Since the pressure at late stages of our evolution has dropped near the minimum value of P at which two phases are present, and in thermal equilibrium at this pressure $n_w \approx 0.1$ cm^{-3} (with $n_c \approx 10$ cm^{-3}), the relative proportions of gas $f_w \approx 0.1$, $f_c \approx 0.9$ in the cold and warm phases are just as expected (with $\bar{n} = 1$ cm^{-3}).

Findings on density and temperature PDFs from other recent TI simulations are varied. From the three-dimensional simulations of Kritsuk & Norman (2002a, 2002b), the late-time (1.5 Myr) mass fractions are $f_w = 0.42$, $f_c = 0.44$ in the stable phases and $f_i = 0.14$ in the intermediate, unstable regime. Kritsuk & Norman use a somewhat different cooling curve from ours, with $n_w = 0.4$ cm^{-3} in thermal equilibrium at the minimum pressure at which two stable phases are available. Since they use $\bar{n} = 1$ cm^{-3}, their result that $f_w \approx n_w/\bar{n}$ is consistent with expectations for a two-phase medium, while the gas at intermediate temperatures appears to be due to mass exchange with the cold medium (see their discussion).

In the one-dimensional simulations of Sánchez-Salcedo et al. (2002) (and using the same cooling curve and mean density as ours), only a few percent of the gas in their "multiple condensation" runs remains at intermediate densities, similar to our results, and their $f_w = 0.3 - 0.4$ at $t \sim 20 - 25$ Myr is similar to our results at comparable (early) times. In the two-dimensional simulations of Gazol et al. (2001) that also include "stellar-like" local heat sources, the late-time mass fractions are $f_w = 0.25$, $f_c = 0.25$, and $f_i = 0.50$. It is not clear to what extent this large proportion of gas at intermediate temperatures is sustained by turbulence (via adiabatic expansion/compression and/or shocks heating or cooling gas that would otherwise be in the warm or cold stable phases), versus being maintained by the localized heating turned on when $n > 15$ cm^{-3}. With three-dimensional MRI simulations in which turbulent driving is "cold," it will be possible to address this important physical issue. (An additional astronomical issue is that since real star formation is confined to giant molecular clouds rather than occurring in a more distributed fashion in cold atomic clouds, localized stellar heating and turbulent driving by expanding H II regions may have limited impact on H I density and temperature PDFs in the real ISM.)

4. *Turbulent driving by TI.*—We find that turbulence produced by "pure TI" has only modest amplitudes, when initiated from "average ISM" pressure and density conditions. For the warm, unstable, and cold phases, respectively, we find typical mass-weighted velocity dispersions of 0.25, 0.35, and 0.15 km s^{-1}. These velocities are all quite subsonic. In simulations starting from thermal equilibrium, Kritsuk & Norman (2002a) similarly find subsonic turbulence ($\mathcal{M}_{\rm rms} \sim 0.3$ at $t <$ 2 Myr), although when gas is initially very hot, supersonic turbulence can be produced. When they include repeated episodes of strong UV heating Kritsuk & Norman (2002b) find Mach number variations $\mathcal{M}_{\rm rms} \sim 0.2 - 0.6$ between "low" and "high" states; since their "low state" is dominated by cold gas with $c_s \sim 1$ km s^{-1}, this is consistent with our results for typical turbulent amplitudes. In the simulations of Koyama & Inutsuka (2002) in which warm gas shocks on impact with a low-density, hot ($T = 3 \times 10^5$ K) layer, TI develops near the interface of shocked gas with the hot medium, leading to the formation of cold cloudlets with velocity dispersions of a few

[3] From Field (1965), this is essentially the geometric mean of λ_F and the product of the sound speed and the cooling time.

km s^{-1}. Although Koyama & Inutsuka attribute this turbulence to the effects of TI, it is possible that other dynamical instabilities associated with the hot/warm interface contribute in driving these motions.

5. *Nonlinear development of axisymmetric MRI.*—We have studied the development of axisymmetric MRI under atomic ISM conditions, both with "TI+MRI" models starting from uniform density and pressure ($P/k = 2000$ K cm $^{-3}$ and $n = 1$ cm^{-3}), and with "cloud+MRI" models that are initiated with the same uniform pressure and total mass, but start with a population of cold clouds embedded in a warm ambient medium. The magnetic field in both types of models is vertical and initially uniform, with $B^2/8\pi = P/1000$. The peak growth rate of MRI (in a uniform medium) is $\Omega/2$, where Ω is the local angular velocity of the galaxy. Since this growth rate is a factor of $\sim$40 lower than typical TI growth rates, the early development of the TI+MRI model is the same as in the "pure TI" model. By the time MRI begins to develop (after a few 100 Myr), the TI+MRI model has similar cloud/intercloud structure—except with more variations in cloud size—to the cloud+MRI model. At early times, the density and temperature PDFs are essentially the same as those produced by TI; at late times, however, while the PDFs remain bimodal, the dense gas is distributed over a somewhat larger range of densities and temperatures, due to the dynamics of the "channel flow" solution (see below).

6. *Spatial scales of MRI in a cloudy medium.*— In both our TI+MRI and cloud+MRI simulations, after a few galactic orbital times, the velocity and magnetic fields become dominated by large-scale structures. Since the smallest-scale MRI mode that would fit in our $L_z = 100$ pc box under *uniform-density* conditions has vertical wavenumber $k = 3$ (in units $2\pi/L_z$; i.e., wavelength $\lambda = L_z/3$), and the fastest growing mode would have $k = 2$, this implies, consistent with expectations, that cloudy density structure in the supporting medium does not grossly alter the character of MRI. We quantify MRI structural development in terms of mode amplitudes of B_y, the azimuthal magnetic field. For the TI+MRI model, the amplitudes of the $k = 1$, 2, and 3 modes are all similar—and motions in the x-z plane continue to be dominated by TI effects, with cloud agglomeration—until $t \sim 400$ Myr, after which the clouds have become highly concentrated and the $k = 1$ MRI mode associated with the "channel solution" (Hawley & Balbus 1992) takes hold. For the cloud+MRI model, on the other hand, the $k = 2$ mode grows first (with clouds remaining small and distributed) and it dominates until $\sim$800 Myr, when the channel solution ($k = 1$) begins to take precedence.

These differences show that the spatial distribution of clouds can have a significant effect on selecting which MRI modes are important. If intercloud distances are small compared to its wavelength, the dominant MRI mode is the same as that predicted for uniform-density conditions. If, however, other turbulent processes acting on scales *small* compared to MRI wavelengths (and times small compared to Ω^{-1}) collect the clouds and correspondingly increase their separations, then only MRI modes at scales larger than twice the typical intercloud distance will be able to grow. As a consequence, for MRI to play an important role in the ISM, either the majority of the gas must remain in a warm, diffuse phase, or else if it collects in clouds their separations must not be too large.

It is interesting to relate these constraints to observational inferences of the H I spatial distribution. From the Heiles & Troland (2003) H I absorption observations that yielded 142 separate cold gas components on 47 lines of sight at $|b| > 10^\circ$, their mean separation would be $\sim$40 pc (taking the cold disk semithickness $\sim$100 pc). The distribution of warm gas is much harder to interpret. According to Heiles & Troland, of the 60% of the H I that is in warm gas, greater than 50% at high latitudes is at lower temperatures than the $T \sim 8000$ K required for approximate pressure equilibrium with the cold clouds; since significant underpressures are difficult to achieve, this gas is likely to be in clouds denser than $\bar{n}$. In the limiting situation in which it is mainly in overdense clouds, and using Heiles & Troland's finding that $\sim$25% of emission components have no associated absorption, the mean distance between clouds would be $\sim$30 pc. Intercloud separations similar to these estimates are small enough that vertical MRI modes could be supported; if cloud spacings are appreciably larger, however, they could not be.

7. *Growth rates and saturation amplitudes of MRI.*—For the low-k modes that are present in both our TI+MRI and cloud+MRI models, typical growth rates are generally comparable to those for modes of the same wavelength in a medium of the same mean density. For the TI+MRI model, typical growth rates are measured to be 0.28 Ω, 0.12 Ω, and 0.18 Ω for the $k = 1$, 2, and 3 modes, respectively, compared to the rates $\gamma/\Omega = 0.45$, 0.5, and 0.41 that would apply for a uniform medium. For the cloud+MRI model, the exponential MRI growth is "cleaner"; rates are $\gamma/\Omega = 0.47$, 0.34, and 0.33 for $k = 1$, 2, and 3 modes, respectively. The growth rates of smaller-scale ($k = 2$, 3) modes are thus slightly more affected by the presence of cloudy structure than that of the largest-scale ($k = 1$) mode, consistent with expectations.

Although definitive results await three-dimensional simulations, these findings provide support for the possibility that MRI may drive turbulence in the diffuse ISM at amplitudes consistent with observations of H I emission and absorption. From previous three-dimensional simulations under relatively *uniform* conditions (accomplished by adopting an isothermal equation of state), the velocity dispersions driven by MRI in steady state were found to be smaller than observed values. In particular, Kim et al. (2003) found that the typical one-dimensional turbulent amplitudes are 3–4 km s^{-1}, whereas the observed nonthermal contribution to the one-dimensional velocity dispersion for both cold and warm gas amounts to $\sigma_v \sim 7$ km s^{-1} (Heiles & Troland 2003). Thus, for a *single phase medium*, MRI-driven turbulent velocity amplitudes in steady state—which are determined by a balance between excitation and dissipation—fall a factor of $\sim$2 short of explaining observations.

Since our present cloudy-medium models show growth rates quite comparable to those in a one-phase medium, the key question is therefore whether MRI dissipation rates are reduced in a cloudy medium, and if so, whether the reduction can yield a factor of 2 increase in σ_v. To see that a quantitative effect at this level is not unreasonable, consider the comparison to an idealized system of $\mathcal{N}_{\rm cl} \equiv l^{-3}$ clouds per unit volume having individual radii r, internal density relative to the mean value $n_{\rm cl}/\bar{n}$, and rms relative velocity dispersion σ_v. With turbulent energy driving and dissipation rates $\dot{\mathcal{E}}_{\rm in}$ and $\sim\sigma_v^2/t_{\rm coll}$, where the collision time $t_{\rm coll} = (4\sqrt{\pi}r^2\mathcal{N}_{\rm cl}\sigma_v)^{-1}$, and σ_v in steady state is an order-unity factor times $(\dot{\mathcal{E}}_{\rm in}l)^{1/3}(n_{\rm cl}/\bar{n})^{2/9}$. For this idealized situation, concentrating material into clouds with $n_{\rm cl}/\bar{n} \sim 30$ (similar to cold ISM clouds) would indeed increase σ_v by a factor of 2 compared to the case with near-uniform conditions, $n_{\rm cl}/\bar{n} \sim 1$. With

three-dimensional simulations, it will be possible to test whether a similar scaling behavior holds for the saturated state of MRI-driven turbulence in cloudy versus single-phase ISM models.

We are grateful to Woong-Tae Kim, Jim Stone, and Mark Wolfire for valuable discussions. This work was supported in part by grants NAG 59167 (NASA) and AST 0205972 (NSF).

REFERENCES

Balbus, S. A., & Hawley, J. F. 1991, ApJ, 376, 214
———. 1992, ApJ, 400, 610
Burkert, A., & Lin, D. N.C 2000, ApJ, 537, 270
Cox, D. P., & Smith, B. W. 1974, ApJ, 189, L105
de Avillez, M. A. 2000, MNRAS, 315, 479
Dickey, J. M., & Lockman, F. J. 1990, ARA&A, 28, 215
Evans, C. R., & Hawley, J. F. 1988, ApJ, 332, 659
Field, G. B. 1965, ApJ, 142, 531
Field, G. B., Goldsmith, D. W., & Habing, H. J. 1969, ApJ, 155, L149
Fitzpatrick, E. L., & Spitzer, L., Jr. 1997, ApJ, 475, 623
Gazol, A., Vázquez-Semadeni, E., Sánchez-Salcedo, F. J., & Scalo, J. 2001, ApJ, 557, L121
Goodman, J., & Xu, G. 1994, ApJ, 432, 213
Han, J. L., Manchester, R. N., & Qiao, G. J. 1999, MNRAS, 306, 371
Hawley, J. F., & Balbus, S. A. 1991, ApJ, 376, 223
———. 1992, ApJ, 400, 595
Hawley, J. F., Gammie, C. F., & Balbus, S. A. 1995, ApJ, 440, 742
Hawley, J. F., & Stone, J. M. 1995, Comput. Phys. Commun., 89, 127
Heiles, C. 2001, ApJ, 551, L105
Heiles, C., & Troland, T. H. 2003, ApJ, 586, 1067
Hennebelle, P., & Pérault, M. 1999, A&A, 351, 309
Jenkins, E. B. 2003, in Proc. JENAM 2002 Workshop, Galaxy Evolution in Groups and Clusters, ed. C. Lobo, M. Serote Roos, & A. Biviano (Dordrecht: Kluwer) in press, (astro-ph/0303266)
Kalberla, P. M. W., Schwarz, U. J., & Goss, W. M. 1985, A&A, 144, 27
Kim, W., & Ostriker, E. C. 2000, ApJ, 540, 372
———. 2001, ApJ, 559, 70
Kim, W., Ostriker, E. C., & Stone, J. M. 2003, ApJ, 595, 574
Korpi, M. J., Brandenburg, A., Shukurov, A., Tuominen, I., & Nordlund, Å. 1999, ApJ, 514, L99
Koyama, H., & Inutsuka, S. 2002, ApJ, 564, L97
———. 2003, ApJ, submitted (astroph-0302126)
Kritsuk, A. G., & Norman, M. L. 2002a, ApJ, 569, L127
———. 2002b, ApJ, 580, L51
Mac Low, M., Balsara, D., Avillez, M. A., & Kim, J. 2001, BAAS, 198, 65.10
McKee, C. F., & Ostriker, J. P. 1977, ApJ, 218, 148
Parker, E. M. 1953, ApJ, 117, 431
Press, W. H., Teukolsky, S. A., Vetterling, W. T., & Flannery, B. P. 1992, Numerical Recipes in C, Second Edition (Cambridge: Cambridge Univ. Press)
Rosen, A., & Bregman, J. N. 1995, ApJ, 440, 634
Sánchez-Salcedo, F. J., Vázquez-Semadeni, E., & Gazol, A. 2002, ApJ, 577, 768
Sellwood, J. A., & Balbus, S. A. 1999, ApJ, 511, 660
Spitzer, L., Jr. 1978, Physical Processes in the Interstellar Medium (New York: Wiley)
Spitzer, L., Jr., & Fitzpatrick, E. L. 1995, ApJ, 445, 196
Stone, J. M., Hawley, J. F., Gammie, C. F., & Balbus, S. A. 1996, ApJ, 463, 656
Stone, J. M., & Norman, M. L. 1992a, ApJS, 80, 753
———. 1992b, ApJS, 80, 791
Truelove, J. K., Klein, R. I., McKee, C. F., Holliman, J. H., II, Howell, L. H., & Greenough, J. A. 1997, ApJ, 489, L179
Vázquez-Semadeni, E., Gazol, A., Passot, T., & Sánchez-Salcedo, J. 2003, in Turbulence and Magnetic Fields in Astrophysics, ed. E. Falgarone & T. Passot (Berlin: Springer), 213
Vázquez-Semadeni, E., Gazol, A., & Scalo, J. 2000, ApJ, 540, 271
Verschuur, G. L., & Magnani, L. 1994, AJ, 107, 287
Wada, K. 2001, ApJ, 559, L41
Wada, K., & Norman, C. A. 2001, ApJ, 547, 172
Wada, K., Spaans, M., & Kim, S. 2000, ApJ, 540, 797
Wolfire, M. G., Hollenbach, D., Mckee, C. F., Tielens, A. G. G. M., & Bakes, E. L. O. 1995, ApJ, 443, 152
Wolfire, M.G, Mckee, C. F., Hollenbach, D., & Tielens, A. G. G. M. 2003, ApJ, 587, 278